

# Multiple wavelength time-of-flight sensor based on time-correlated single-photon counting

Gerald S. Buller,<sup>a)</sup> Ross D. Harkins, Aongus McCarthy, Philip A. Hiskett,<sup>b)</sup> Gordon R. MacKinnon, George R. Smith, Raymond Sung, and Andrew M. Wallace  
*School of Engineering and Physical Sciences, Heriot-Watt University, Riccarton, Edinburgh EH14 4AS, United Kingdom*

Robert A. Lamb, Kevin D. Ridley, and John G. Rarity<sup>c)</sup>  
*QinetiQ Ltd., St. Andrews Road, Malvern, Worcs, WR14 3PS, United Kingdom*

(Received 20 April 2005; accepted 17 June 2005; published online 3 August 2005)

This article describes a time-of-flight sensor based on multiple pulsed laser sources which utilizes time-correlated single-photon counting. The sensor has demonstrated good performance at ranges of up to 17 km in daylight conditions. Analysis techniques were developed to examine the returns from targets containing more than one scattering surface. © 2005 American Institute of Physics.  
 [DOI: 10.1063/1.2001672]

## I. INTRODUCTION

This article describes a multiple-wavelength time-of-flight sensor based on time-correlated single photon counting (TCSPC). We have used this technique previously<sup>1,2</sup> in the application of three-dimensional imaging at ranges of less than 50 m. The use of multiple wavelengths widens the scope and functionality of photon counting, allowing issues such as: the wavelength dependence of temporal resolution, simultaneous multichannel data acquisition, atmospheric propagation, the wavelength dependence of speckle, and the wavelength dependence of target reflectivity to be studied in a single integrated LIDAR system. Of particular interest is the detection and analysis of signatures from distributed targets (range profiling). This is particularly important for space applications, for example, laser altimetry of planet and asteroid surfaces, where precision range resolution at a distance is required.

In this article the design of the LIDAR system is described and its performance is assessed from test data from two corner cubes separated by a variable and known distance (9–25 cm). The separation is measured using TCSPC. The corner cubes were positioned at variable ranges from 215 m to 17 km but only a selection of data that illustrates the main points are presented in Secs. IV. We describe the optomechanics used in the transmission of six discrete wavelengths, signal acquisition, wavelength separation, detection, and data analysis. A schematic of the system is shown in Fig. 1. This diagram illustrates the modular construction of

the system, with each major component described in Sec. II and III of this article. Experimental results are discussed in Sec. IV.

## II. OPTICAL SETUP

### Optical design and optomechanics

The optical system was based around a commercially available Meade LX200 catadioptric Schmidt–Cassegrain telescope,<sup>3</sup> with additional custom-made optomechanical components. These consisted of three main assemblies:

- output: a support ring for mounting six pulsed diode lasers, of different wavelengths, around the circumference of the telescope aperture;
- collection: an assembly for attaching and positioning a collection fiber and camera in the image plane of the telescope; and
- optical routing: an optical routing module, based on a diffraction grating approach, was used to spatially separate the six wavelengths of the return signal and route each discrete wavelength to a dedicated specific single-photon detector.

Most of these assemblies were manufactured from aluminum alloy (HE 30 TF). All of the mechanical design work was carried out using a three dimensional computer-aided design (CAD) software package. The completed CAD models were exported to a three-axis continuous numerical control (CNC) milling center for manufacture. The machined aluminum was surface finished with a 10  $\mu\text{m}$  thick black anodized coating. The coating helped reduce wear and damage to the components while handling and minimized stray light levels.

### 1. Optical signal output and collection assemblies

The custom-made output and collection assemblies of the system were attached to a 200 mm diam aperture, Meade LX200 telescope. The layout of the assemblies is shown

<sup>a)</sup> Author to whom correspondence should be addressed; electronic mail: g.s.buller@hw.ac.uk

<sup>b)</sup> Present address: Los Alamos National Laboratory, Mail Stop D454, P.O. Box 1663, Los Alamos, NM 87545.

<sup>c)</sup> Present address: Dept. of Electrical & Electronic Engineering, University of Bristol, Merchant Venturers Building, Woodland Road, Bristol BS8 1UB, UK.

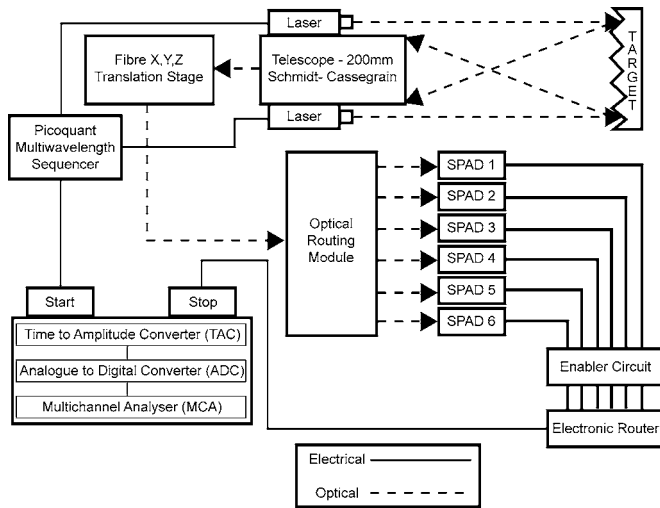


FIG. 1. Schematic of multiple wavelength time-of-flight sensor illustrating the integration of the telescope, optical routing module, multiwavelength sequencer, fiber translation stage, the enabling circuit, the router, and the SPC-600 (time to amplitude converter, analog to digital converter, and multichannel analyzer).

schematically in Fig. 2. Six laser diodes were chosen operating at wavelengths of 630, 686, 780, 841, 911, and 975 nm. This choice was dictated, in part, by commercial availability, cost, compatibility with the spectral responsivity of silicon based single photon detectors and the desire to cover as much of the near infrared as possible. Wavelength choice was further limited by the reduced quantum efficiency of the detectors for  $\lambda > 950$  nm. The diodes were spaced at  $60^\circ$  intervals around the outer circumference of the telescope aperture using a custom-made ring that incorporated a separate kinematic mount for each diode. Each mount had retaining springs and two 0.5 mm pitch thread screws that provided pitch and yaw adjustment of the diode and independent alignment of each laser onto a target. The retaining springs were sufficiently stiff to prevent misalignment due to accidental knocks. When the target was in the field of view of the telescope, these mounts enabled the output beams of the diodes to be easily and accurately aligned onto the target. In normal operating conditions the alignment was stable—only requiring minor adjustments when the setup was moved and reassembled at a new location. In each case, the six laser diodes were adjusted to a nominally eye-safe continuous

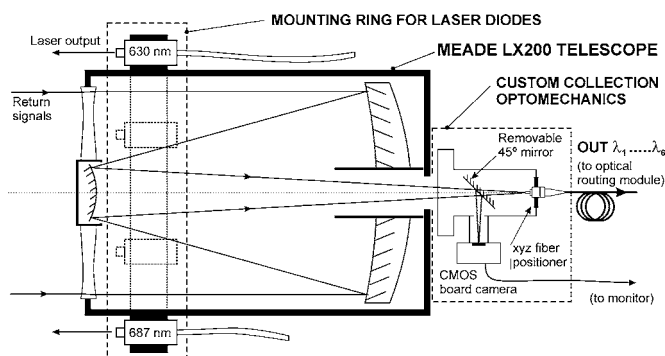


FIG. 2. Schematic drawing of the adapted Meade Schmidt-Cassegrain telescope showing the position of the mounting ring for the laser diodes and an outline of the collection arrangement.

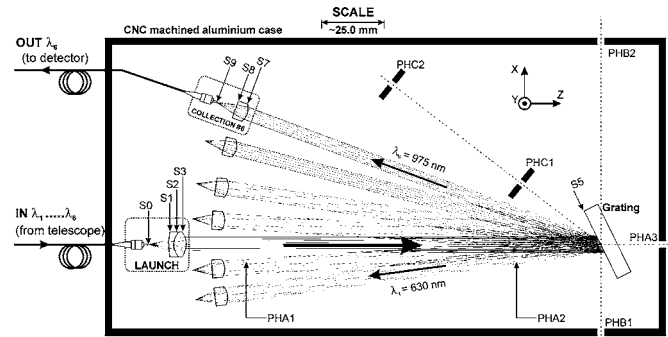


FIG. 3. Schematic diagram showing a plan view of the optical routing module indicating the surfaces (S0–S9) included in the ray trace model for each wavelength channel, and the positions of the alignment pinholes (PHxx). The fiber-coupled lens assembly labeled Collection No. 6 is replicated for each of the other five output channels.

power level of  $100 \mu\text{W}$ . In the case of the measurements presented in this article, the lasers were operated at repetition rates of 6.67 and 3.33 MHz, which correspond to pulse energies of  $\sim 15$  and  $\sim 30$  pJ for each wavelength.

The telescope collected the reflected signal from the target and focused it onto an optical fiber core. This fiber was positioned in the image plane of the telescope using a custom-made assembly which was attached to the telescope in place of the supplied eyepiece and included a camera port as well as the fiber positioning mechanism. The camera was used, in conjunction with a removable  $45^\circ$  mirror on a kinematic mount, to align the telescope and laser beams on a distant target. Focusing of the telescope was achieved using the built-in adjustment on the telescope. Once aligned, the mirror was removed and the fiber positioning mechanism allowed precise adjustment of the fiber core along the  $xyz$  axes by means of three screw adjusters. Having an independent  $z$ -axis adjustment from that of the focus of the telescope gave greater control over the alignment of the fiber in the image plane. Springs were incorporated into the mechanism to minimize backlash. An FCPC connectorized fiber patchcord coupled the output from the telescope to the optical routing module described next.

## 2. Optical routing of the return signals

The fiber from the telescope was connected to the input port of a custom-made optical routing module. The optical router took the six-wavelength output from the fiber and spatially demultiplexed it into six separate fibers, one for each wavelength channel, which were connected to the six single-photon detectors. The optical routing was achieved using a diffraction grating, as shown schematically in Fig. 3. The optical design of this optical routing system was ray traced using a commercially available software package. Prior to performing the design stage, the peak wavelengths of the laser diodes were measured and confirmed against the manufacturer's specification.

The optical routing module's launch unit indicated in Fig. 3 consisted of a 9 mm diam, 12 mm effective focal length achromatic lens (surfaces S1–S3) to collimate the output from the fiber. The fiber and lens were housed in a custom-designed package with a fine pitch screw adjustment

for positioning the fiber relative to the lens along the optic axis. The launch unit of the optical routing module was mounted on a custom  $xy$  tilt and yaw adjustable optomechanical stage.

The collimated output beam from this lens had a nominal diameter of 6 mm and was directed onto a plane-ruled reflectance grating approximately 200 mm away (labeled  $S5$  in Fig. 3). The grating was written on a  $30 \times 30 \times 6$  mm thick BK7 glass substrate and was used to separate the six wavelengths in the horizontal plane. The grating had a ruled area of  $26 \times 26$  mm with 1200 grooves/mm and a blaze wavelength of 760 nm with a blaze angle of  $26.7^\circ$ . The optomechanical mount for the grating had  $x, z$ , roll, pitch, and yaw adjustments.

The collection module indicated in Fig. 3 was based on a commercial FCPC fiber-coupler package. This package consisted of steel housing for the lens with a built-in FC fiber connector. The lens, indicated by surfaces  $S7$  (aspheric) and  $S8$  (plano) in Fig. 3 had a diameter of 6.4 mm and an effective focal length of 11 mm at 633 nm. The package fitted to a custom kinematic mount that incorporated  $xy$ , tilt, and yaw adjustments. The six individual collection modules were, in turn, mounted accurately in position on a CNC machined positioning frame that was fixed to the base of the optical routing module. Steel pins were used to provide accurate alignment between these components.

The ray tracing software was used to determine the optimum angle of incidence of the launch beam on the grating. This was done to position the launch beam midway between channels 2 and 3, since these were the adjacent channels with the largest wavelength difference, i.e., 94 nm. The distances from the grating to the collection units (i.e., the distances between surfaces  $S5$  and  $S7$ ) were chosen so that there was sufficient space to accommodate the optomechanics as well as provide access for making the adjustments required for each unit.

According to the manufacturer's specification, the fiber collimation/coupling packages were supplied prealigned for a wavelength of 633 nm. This corresponded to the lower end of the range of wavelengths used in this system and meant that the longer wavelengths focused behind the focal plane for 633 nm, resulting in larger spot sizes with increasing wavelength. The image distance at a wavelength of 633 nm was determined by ray-tracing techniques to be 7.88 mm. This distance was then used as the fixed image distance for all of the other zoom positions, and diffraction based spot sizes for each of the channels were calculated for this plane using the ray-tracing software. The launch beam, the grating, and the individual collection modules for each channel were aligned with the aid of pinholes, mounted in the positions indicated in Fig. 3 and an external He:Ne laser beam.

The optical routing module had optical losses ranging from 2.7 dB at the 630 nm wavelength channel and increasing to 10 dB at the 975 nm wavelength channel. These increasing losses were found to be consistent with ray-tracing analysis of each wavelength channel—the increasing wavelength meant increasing optical aberrations and associated

defocus errors. This was, of course, consistent with the pre-alignment of the collimation/coupling packages at a wavelength of 633 nm.

A schematic of the multiple wavelength sensor is shown in Fig. 1. The six wavelengths used in the system were chosen to provide a wide range of wavelengths to test spectral and temporal response. A laser driver sequencer triggered the six lasers independently and in sequence, thus each laser operated at a pulse repetition rate of  $1/6$  of the trigger rate. The pulses from each of the six lasers were reflected from the target back to the telescope aperture, and the telescope focused the collected light onto the fiber. The collected signal photons were then transmitted via the collection fiber patchcord to the optical routing module where they were separated into their individual wavelengths and detected by six individual Si single-photon avalanche diode (SPAD) detectors via optical fiber patchcords. Fibers with angled cleaves were used to minimize spurious multiple reflections that could be measured by the single-photon detectors. These single-photon avalanche diodes are discussed later in Sec. III B.

The system optics were designed in order to maximize the photon return, while maintaining negligible crosstalk between wavelength channels and reducing the detected ambient light detected to a minimum. In field trials corner cubes of various aperture sizes, and therefore cross section, were used. Corner cubes are convenient retroreflectors but they reflect light back to the source, i.e., the laser diodes themselves, and not strictly back to the telescope aperture. This is particularly evident at short range where the reflection partially overlaps the entrance aperture of the telescope, leading to a loss in signal. During daytime operation when the ambient light level was relatively high, alignment was more difficult. This was particularly so at the longer wavelengths where the detector efficiency was significantly reduced. In order that optimum alignment could be achieved at long distances, it was necessary to initially use retroreflectors at approximately half the range distance, and then align on the full distance. The angular field of view of the telescope was  $25 \mu\text{rad}$  (half angle) according to the manufacturer's specifications. To a first approximation, this gives an indication of the angular alignment accuracy necessary for the telescope.

### III. ACQUISITION ELECTRONICS

#### A. Timing electronics

TCSPC is a statistical sampling technique with single photon detection sensitivity, capable of picosecond timing resolution.<sup>4</sup> The detectors used in our photon counting experiments are silicon-based SPAD detectors. The general advantages of using SPADs are that these detectors exhibit superior photon detection efficiency and a faster time response compared with photomultipliers. These detectors provide the stop output for the time to amplitude converter (TAC) in response to the arrival of the first photon scattered from the target for each laser pulse. The trigger is provided by a synchronized output from the laser driver. This provides a reference electrical pulse and represents the start for the TAC.

A constant fractional discriminator (CFD) circuit was used to differentiate between levels of electrical signals. The

TAC produces an analog signal which is proportional to the difference in time between the stop and start signals, and subsequently this output signal is digitized by an analog-to-digital converter (ADC). The multichannel analyzer (MCA) increments the contents of a memory address at a location corresponding to this time difference. The procedure is then repeated thousands of times for many laser pulses, until the MCA builds up a probability histogram of the photon arrival times.

Data are represented graphically in real time and probability histograms are displayed as counts against time. The CFD, TAC, ADC, and MCA are integrated into a plug-in card (Becker and Hickl SPC-6005) for a standard IBM-compatible PC. The MCA comprises 4096 time bins, hence for a TAC range of 25 ns this corresponds to 6.1 ps/bin. Up to 34 histograms may be acquired simultaneously, however in our work only six were activated, one for each wavelength. When a TCSPC system records the arrival time of a single photon at a SPAD with respect to a synchronous timing signal, “aliasing” may occur. In the case of a time-of-flight system, this synchronization pulse can be provided from an APD, which detects a fraction of the outgoing laser pulse.<sup>5</sup> An alternative approach is to use the electrical synchronization pulse from the laser driver. At the time of emission of a laser pulse, there will be an electrical synchronization pulse, which we can denote as the “paired” synchronization pulse. It is desirable that when the SPAD detects a single photon from the pulse that the “paired” synchronization pulse is used as the time reference because it minimizes “jitter” (an uncertainty in the timing of an event). However, for long ranges several synchronizing pulses will be emitted before the arrival of the first reflected pulse, resulting in possible increased jitter during the time-of-flight. One simple method to obtain “pairing” is to direct the electrical synchronization pulses via a passive delay equivalent to the time-of-flight of the laser pulse. Passive delays are preferred to active delays because they do not contribute significantly to the “jitter,” although they can significantly attenuate the electrical pulse. In this application for target ranges of  $\leq 2$  km, we used the synchronous electrical signal from the laser driver in conjunction with an appropriate passive delay—i.e., a “paired” pulse approach. For ranges greater than 2 km, the length of delay necessary meant it was not possible to use the “paired pulse” approach, hence the TAC start signal derived from the electrical synchronization pulse from a later laser pulse. This approach compromised the jitter for distances of  $>2$  km, however this effect is difficult to quantify given the increased effects of turbulence at these distances (see below).

## B. Single photon avalanche diodes

A SPAD is an avalanche photodiode reverse-biased at electric fields greater than that of the avalanche breakdown field, in the Geiger mode regime. This produces very high gain, resulting in single-photon sensitivity. Diode structures suitable for use as SPADs have been successfully implemented in silicon, and other material systems such as germanium<sup>6</sup> and III–V semiconductors<sup>7</sup> have been investigated. The SPADs used in this work were fabricated from

silicon, and are commercially available from Perkin–Elmer. These SPADs are packaged with a fiber input stage and include quenching and pulse shaping circuitry.

The silicon SPADs used in these experiments have a detection efficiency of approximately 60% at 630 nm wavelength, which reduced to approximately 10% at 980 nm. The dark count rate was approximately 150–250 counts/s, however the choice of detector dark count rate had little significance in this application, due to the presence of high ambient light levels (see below). The jitter times (temporal resolution) of the SPADs are 400–700 ps full-width-at-half-maximum (FWHM).

## C. Enabler circuit

The enabler circuit was designed to reduce the effect of ambient light on the measured photon return signal. This is particularly important in LIDAR applications where a high uncorrelated solar background can dominate the signal return. The system used six SPAD detectors connected via an electronic router to an SPC600 counting card. The function of the electronic router is to pass timing pulses from several single-photon detectors to the acquisition card in order that these signals could be recorded independently. The arrival times of the laser photons can be predicted within a well-defined time window. Background noise events, which in this application are mainly due to the ambient in-band solar background, occur randomly in time, and cause the loss of wanted signals due to the finite dead time of the SPC600 card. This is particularly evident with high background signal levels, as is the case in this application. This is an unusual situation in photon-counting applications and leads to further issues with the electronic router. It was evident that the high background signal on the photon-counting detectors led to crosstalk as the counts from one wavelength channel were counted in the histogram of another. This, of course, led to a decrease in the apparent signal-to-background ratio. By enabling the output signals from a particular detector only when the signal return is expected, solar background counts due to detection by the other five detectors could be eliminated. Of course, background noise from within the time window of interest originating from the enabled detector will still be acquired, but this approach leads to more efficient data collection and greater signal to noise.

The output of each detector was connected to one input of a two-input NAND logic gate. The other input of each gate was used to turn the gate on and off. The enabler generated the “on-off” control signals in sequence using the clock common to the rest of the system to achieve synchronization. The “on” time can be trimmed to values less than one clock period to further reduce the amount of background noise in the system. The temporal alignment of the on period for each detector is achieved by manually skipping whole clock periods until it coincides with the time correlated events from that detector. Further fine tuning of the timing within one clock period can be achieved by varying the length of electrical lead used to carry the clock to the enabler.

The timing diagrams shown in Fig. 4 illustrate the processes involved in removing unwanted background photons, with no loss of wanted signals of interest for a specified time

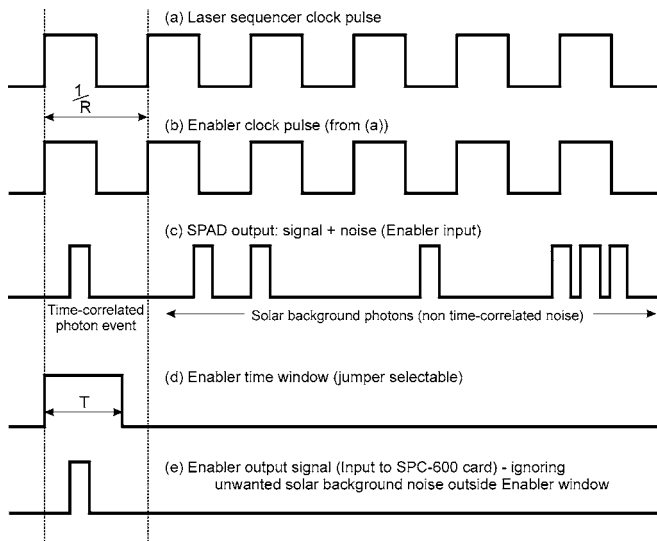


FIG. 4. Timing diagrams illustrating the removal of unwanted background noise with no loss of signal. In (a) we have the laser sequencer clock pulse (shown here for all six lasers), with a different laser pulsing sequentially, for each period. The period is proportional to the reciprocal of the laser repetition rate,  $1/R$  (typically,  $R=20$  MHz and  $1/R=50$  ns) which provides a timing reference enabler clock pulse, seen in (b). The output of the SPAD, including noise signals, is seen in (c) before going to the enabling circuit. In (d) the enabling circuit provides an adjustable time window (jumper selectable from 5 to 50 ns in 5 ns steps), which must lie within the period of the clock, and is active for one clock period in every six. In (e) the enabler, upon receiving the raw output signal of the SPAD, ignores timing events outside the enabler time window, and hence the reference timing window of the laser sequencer clock period, therefore resulting in the removal of the unwanted background photocounts, the result being that the laser photon events remain intact, with all random background photocounts (outside the enabler time window) removed giving a higher signal to noise ratio overall. The random background light contribution has effectively been reduced by  $5/6$ .

window (the enabler time window), with the result that only photons that are in the measurement time window of interest were recorded. Figure 4(b) shows the enabler pulse [taken as a reference from the clock that drives the lasers (a)] of six clock periods, which is matched with the sequencer clock pulse. Therefore the clock provided by the sequencer acts as a reference for the enabler clock, with each pulse period proportional to the reciprocal of the laser repetition rate  $1/R$  as shown in the diagram. In Fig. 4(c) we can see the raw output of the SPAD (laser signal returns and solar background counts) before inputting to the enabler to remove unwanted random background photocounts. The enabler circuit works by only opening a timing window of one clock period in every six, since measurements of interest can only occur in this specific timing window—therefore, photocounts from just before the window of interest do not contribute to increased dead time in the detection system. Photon events inside the window originating from the other five detectors do not contribute to the noise in that measurement. Since the enabler permits only those photons acquired in a detector's predicted time window (i.e., when that particular wavelength channel's return signal is expected), then the background count level is reduced by a factor of approximately 6 compared to the case of not using an enabler circuit. Figure 5 shows the comparison between data collected without the enabler and data taken with the enabler. It is evident that

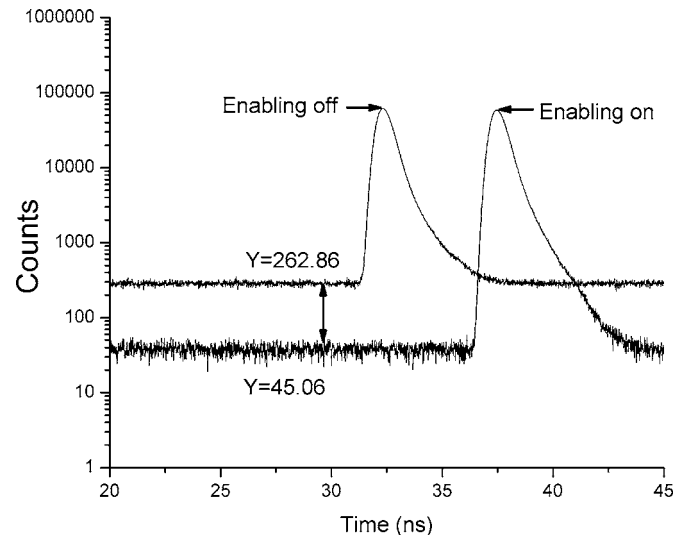


FIG. 5. Comparison between photocounts taken with and without the enabler circuit and the improved signal to background ratio on a semilogarithmic plot. It can be seen that the background contribution of the counts is collected with and without the enabling circuit. The background without enabling is  $\sim 263$  counts, and the solar background with enabling gives  $\sim 45$ , for the same experimental conditions.

with the enabler, the background has been reduced significantly, without significantly reducing the number of signal counts. The measured background noise for the black curve was  $\sim 263$  counts, and the background for the red curve was  $\sim 45$  counts, thus implying that the background contribution for the red curve has been reduced by the ratio  $263/45 \sim 6$ , as expected.

Note that in the measurements shown in Fig. 6, it was necessary to temporally align the measurement window in order to observe the photon return signal. This was achieved by implementing a macro delay in the enabler circuit. Another practical consideration is the limitation imposed by the maximum frequency at which the enabler circuit can operate. In our design the maximum frequency was 40 MHz. Since the reference clock period provides the timing window, operating at repetition rates greater than 20 MHz produced unwanted edge effects.

#### IV. EXPERIMENTAL RESULTS

Example results from a corner cube reflector at a range of 2 km are shown in Fig. 6. This shows the temporal response for the six different wavelengths and the background level caused by leakage of the ambient daylight. The background level is different in each case because the optical throughput varies spectrally across the six channels due to varying diffraction efficiency and choice of multimode fiber core diameter at the outputs of the optical routing module.

Problems that can be encountered when taking measurements at this range include beam scatter, scintillation, and atmospheric loss. Beam scatter is due to atmospheric aerosols. This phenomenon would manifest itself as a significant reduction in photon return count rate. Scintillation, caused by turbulence, causes the total count rate to fluctuate and is particularly significant at short duration acquisition periods. Scintillation is observed as a twinkling appearance of the

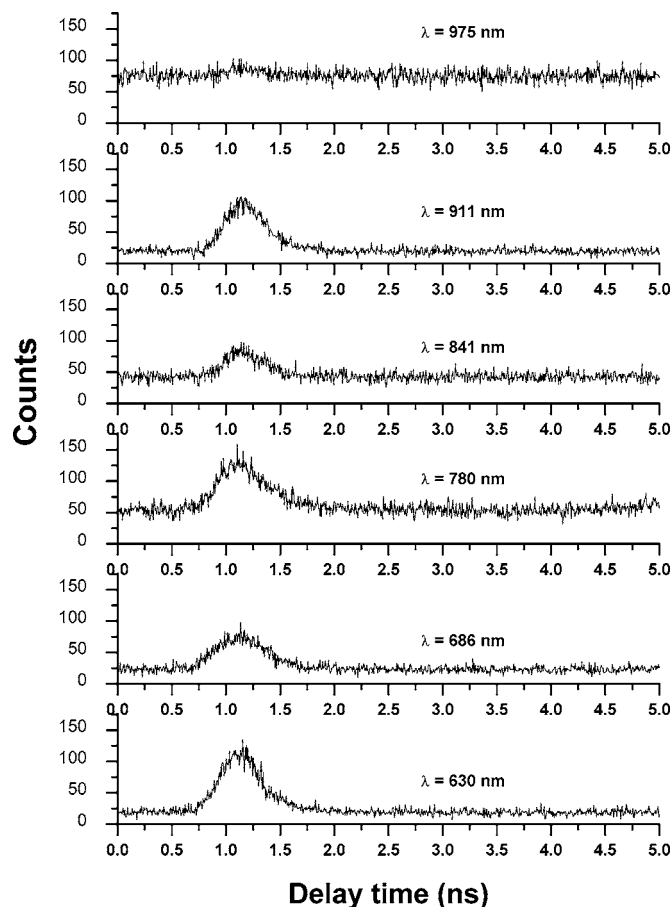


FIG. 6. Example of sensor response for each of the six wavelength channels. In this case, six simultaneous measurements at each laser wavelength were made for a target at a distance of 2 km. Note the background level is different in each case.

return signal, particularly from a retroreflecting target. Turbulence induced beam wander and image tilt may also produce fluctuations. These effects produce fluctuations in the signal count for short acquisition times. This will depend on the total acquisition period, the atmospheric conditions, and the range. An example of the effect of scintillation is shown in Fig. 7 for two returns measured under identical conditions, measured a few seconds apart.

It is important to note that the choice of wavelengths was such that the operating wavelengths were not resonant with the expected molecular absorption bands.<sup>8</sup> By careful choice of the fiber core diameter used in that patchcord between the telescope and the wavelength separator, it was possible to substantially improve the signal-to-background ratio, without significantly affecting the signal return. The fiber core diameter that showed the best achievable signal with minimal solar background was in the range  $10 \mu\text{m} \leq d \leq 50 \mu\text{m}$ . In these experiments, a  $50 \mu\text{m}$  fiber core diameter was chosen for ease of alignment and to mitigate the effect of turbulence in the focal plane of the telescope.

## V. DATA ANALYSIS: LOCATING AND CHARACTERIZING MULTIPLE PEAKS IN PHOTON COUNT HISTOGRAM DATA

In general, we use the multispectral system to provide information about the range, spatial, and spectral distribution

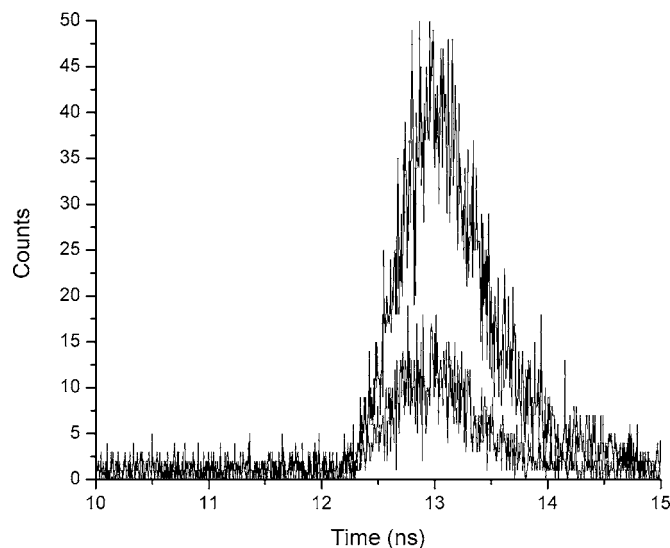


FIG. 7. Two measurement responses taken using 3# in. corner cube at a range distance of 17 km which demonstrate the effect of scintillation on the return signal. The integration time used was 100 ms, each set of measurements were taken for ten runs at a particular integration time, and the count rates vary significantly for shorter integration times than they do at longer integration times.

of a target signature. We have evaluated the system response using corner cubes and noncooperative targets in the range 200 m–17 km, including distributed targets with effectively more than one target surface. Using single or pairs of corner cubes, we are sure of obtaining one or two clearly defined returns that we can use to perform tests on the system depth resolution.

Interpretation of the histogram is a two-stage approach.<sup>9</sup> First, we use nonparametric testing of the histogram to find initial estimates of possible peaks in the histogram data. This is effectively a “bump-hunting” process, but in contrast to earlier work that looked for zero crossings in the first derivative to locate modes,<sup>10</sup> we analyze the first and second derivatives to find both modes and cotangents, since returns in close proximity may not lead to distinct modes. In the second stage, we apply constrained nonlinear optimization using sequential quadratic programming to find the Poisson maximum likelihood estimate<sup>11</sup> of the number of peaks, with their respective positions and amplitudes. To initialize an operating model of the shape parameters of the photon count distribution we can use a reference signal from a corner cube or a “good” external target if available, if not we use a generic model. This is used only to give an initial estimate, or even a fixed set of shape parameters, i.e., an instrumental response. During optimization, we can either allow these shape parameters to vary or keep them fixed, dependent on the reliability of the *a priori* knowledge.

We can illustrate the data analysis on a number of real measurements from the multispectral lidar system. In Fig. 8, we show two examples from the scintillation data obtained at a standoff distance of 17 km. In each case the integration time was 0.1 s and the 631 nm wavelength channel was used. Analysis of the peak parameters shows for Fig. 8(a) a peak amplitude of 31.09 counts at 634.41 time bins, with a background of 0.99 counts, and for Fig. 8(b) a peak amplitude of

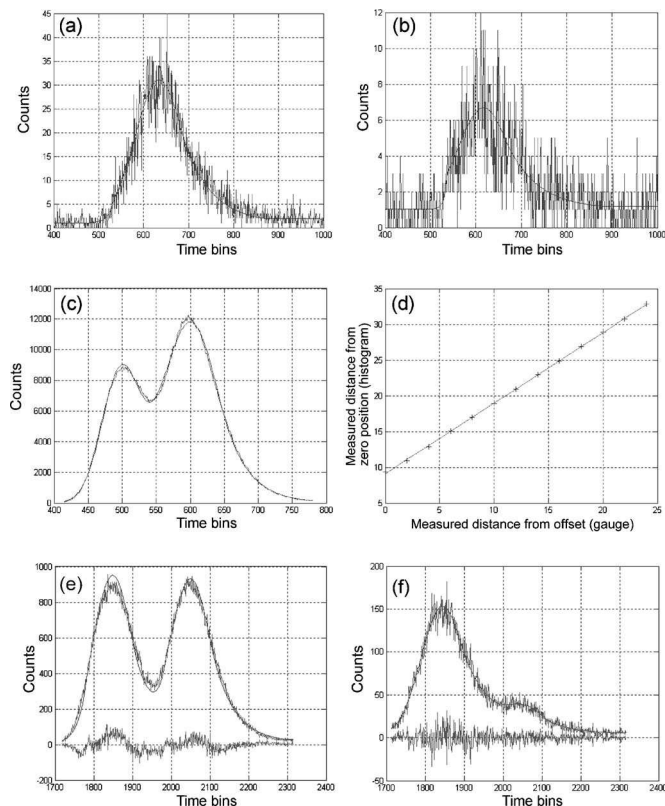


FIG. 8. (a) and (b) Two examples of returns fitted to scintillation data at 17 km with a collection time of 0.1 s; (c) two well-defined modes at the minimum separation of the corner cube measurement at 330 m; (d) variation of laser against gauge measured corner cube separation with respect to an offset of 9.1 cm; (e) 630 nm wavelength; and (f) 780 nm wavelength. Two examples of returns from matt targets at a distance of 330 m.

6.71 counts at 617.07 time bins with a background of 1.03 counts, i.e., an apparent shift of 17 bins (104 ps) between the two measurements. Increasing the collection time to tens of seconds reduced this effect. However, as described in Sec. III, increased jitter can also be caused by “unpaired” synchronous pulses. To obtain a more systematic estimate of the target resolution of the system in the comparative absence of scintillation effects we placed a pair of reflecting corner cubes in the path of the beam at a range of 330 m and collected data for 10, 20, and 30 s. The separation of the fitted peaks gives a measure in time that can be compared to the true distance separation. Figure 8(c) is an example in which two well defined modes are visible at a nominal separation of 9.1 cm, the minimum separation allowed by the

mounting apparatus that included a graduated scale to provide ground truth. Figure 8(d) shows the excellent correspondence between the laser measured separation and the ruled gauge measurement; a regression fit to the line is  $y=9.09+0.99x$  (cm), with a mean absolute error of 0.6 mm between the two measurements, i.e., within the tolerance of the ruled measurement. However, the absolute range accuracy is determined by the number of counts and the intrinsic jitter of the photon detectors ( $\sim 700$  ps corresponding to a range resolution of  $\sim 100$  mm). The final two examples show real data from matt target surfaces, in fact from a model truck and a model figure of a sphinx at a distance of 330 m. The difference between the two spectral channels, i.e., 631 and 780 nm is immediately apparent. The respective peak positions and heights at 630 nm are 152.92 counts at 1845.25 bins and 25.77 counts at 2059.89 bins. The respective peak positions and heights at 780 nm are 950.44 counts at 1848.95 bins and 896.70 counts at 2052.29 bins. This illustrates both the capability of the system to resolve multiple peaks, and the informative nature of the multispectral capability.

## ACKNOWLEDGMENTS

The authors wish to thank Dr. C. A. Ayre (Defence Science and Technology Laboratories, Fort Halstead) and Clive R. Foster (QinetiQ, Fort Halstead) for useful discussions.

- <sup>1</sup>J. S. Massa, A. M. Wallace, G. S. Buller, S. J. Fancey, and A. C. Walker, *Opt. Lett.* **22**, 543 (1997).
- <sup>2</sup>S. Pellegrini, G. S. Buller, J. M. Smith, A. M. Wallace, and S. Cova, *Meas. Sci. Technol.* **11**, 712 (2000).
- <sup>3</sup>Meade Instruments Corporation, LX Series of telescopes. ([http://www.meade.com/catalog/lx/lx\\_series.html](http://www.meade.com/catalog/lx/lx_series.html))
- <sup>4</sup>M. Umasuthan, A. M. Wallace, J. S. Massa, G. S. Buller, and A. C. Walker, *IEE Proc. Vision Image Signal Process.* **145**, 4 (1998).
- <sup>5</sup>J. S. Massa, G. S. Buller, A. C. Walker, G. Smith, S. Cova, M. Umasuthan, and A. M. Wallace, *Appl. Opt.* **41**, 1063 (2002).
- <sup>6</sup>G. S. Buller, S. J. Fancey, J. S. Massa, A. C. Walker, S. Cova, and A. Lacaita, *Appl. Opt.* **35**, 916 (1996).
- <sup>7</sup>P. A. Hiskett, J. M. Smith, G. S. Buller, and P. D. Townsend, *Electron. Lett.* **37**, 1081 (2001).
- <sup>8</sup>P. I. Eardley and D. R. Wilson, *IEE Proc.: Optoelectron.* **6**, 143 330 (1996).
- <sup>9</sup>A. M. Wallace, R. C. W. Sung, G. S. Buller, R. D. Harkins, R. E. Warburton, and R. Lamb (unpublished).
- <sup>10</sup>P. Chaudhuri and J. S. Marron, *J. Am. Stat. Assoc.* **94**, 807 (1999).
- <sup>11</sup>M. D. Hannam and W. J. Thompson, *Nucl. Instrum. Methods Phys. Res. A* **431**, 239 (1999).